POLITECNICO DI TORINO
Repository ISTITUZIONALE

# Ag nanoparticle-based inkjet printed planar transmission lines for RF and microwave applications: considerations on ink composition, nanoparticle size distribution and sintering

*Original*
Ag nanoparticle-based inkjet printed planar transmission lines for RF and microwave applications: considerations on ink composition, nanoparticle size distribution and sintering time / Chiolerio, Alessandro; M., Cotto; P., Pandolfi; P., Martino; Camarchia, Vittorio; Pirola, Marco; Ghione, Giovanni. - In: MICROELECTRONIC ENGINEERING. - ISSN 0167-9317. - STAMPA. - 97:9(2012), pp. 8-15. [10.1016/j.mee.2012.03.036]

*Availability:*
This version is available at: 11583/2496075 since:

*Publisher:*
Elsevier

*Published*
DOI:10.1016/j.mee.2012.03.036

*Terms of use:*

This article is made available under terms and conditions as specified in the corresponding bibliographic description in the repository

*Publisher copyright*

(Article begins on next page)

25 April 2024

# Ag nanoparticle-based inkjet printed planar transmission lines for RF and microwave applications: considerations on ink composition, nanoparticle size distribution and sintering time

A. Chiolerio[1,4], M. Cotto[2], P. Pandolfi[2], P. Martino[2], V. Camarchia[3,4], M. Pirola[3], G. Ghione[3]

[1] Applied Sciences and Technology Department, Politecnico di Torino, Corso Duca degli Abruzzi 24, IT-10129 Torino, Italy

[2] Politronica Inkjet Printing S.r.l., Corso Castelfidardo30/A, IT-10129 Torino, Italy

[3] Electronic and Telecomunication Department, Politecnico di Torino, Corso Duca degli Abruzzi 24, IT-10129 Torino, Italy

[4] IIT, Italian Institute of Technology @ POLITO, Center for Space Human Robotics, Corso Trento 21, IT-10129 Torino, Italy

## Abstract

Sintering of Ag Nanoparticle (NP) – based inkjet printed tracks is a crucial process for the next-generation digitally printed electronics. In particular, while the digital printing, as additive technology, is now well settled for what concerns either DC or signal applications both on rigid and on flexible substrates, this technology has not been demonstrated yet in the RF or microwave field, and a few works appear considering vacuum-evaporated films, screen-printed pastes or inkjet printed inks. We studied the effects of both ink composition and thermal profile on the resulting electrical properties, performing real-time resistance acquisition (DC) and post-annealing microwave measurements. We tested ink compositions featuring both different NP size distributions and different phase compositions, including a pure solvent/salt/metal one and a solvent/salt/metal/polymer one, resulting in a peculiar mass distribution and heat diffusion. The composition strongly affects the onset of electrical percolation and the final resistivity; on the contrary, the heating rate can either have an effect on electrical properties or not depending on the composition. The microwave characterization of microstrip lines printed on alumina substrates, performed up to 26.5 GHz, yield attenuations that are comparable with the best results obtained so far with the same technology.

**Keywords:** inkjet printing, silver nanoparticles, real-time measurements, microwave planar transmission lines

# 1. Introduction

Inkjet printing technology has raised a great interest for information technology electronic applications, due to its high throughput and low costs. The possibility of realizing quite high resolution conductive lines on flexible substrates, with a simple additive process, is extremely attractive but poses some problems that still have to be solved. In particular, it may be questioned whether such materials have adequate high-frequency performances for analog RF or microwave applications (as an example, for the manufacturing of low-cost RFID tags or printed planar antennas) with respect to conventional materials like Cu or Au films. In the present paper we address the issue of the high-frequency behavior of Ag nanoparticle (NP) films.

As well known, after inkjet printing of an Ag NP-based ink, a thermal treatment to promote NP adhesion and coalescence and obtain electrical percolation must be performed. It can be done either with hot plate or oven [1] driven by conduction/convection mechanisms, or with a laser [2] or a microwave oven [3] driven by radiation absorption mechanisms. Mixed approaches have been developed. Generally, thermal sintering requires quite high temperatures starting from 220 to 250 °C [4,5]. New processes based on flash sintering [6], plasma [7], electrical [8], chemical induced sintering [9] or metallorganic ink decomposition [10] have been also proposed, producing results which are not yet satisfactory from the point of view of the final resistivity. Among the best results in ultimate electrical performance, 53% of the silver bulk conductivity was obtained by applying a compressive stress of 5 MPa and a temperature of 250 °C [11], while the authors obtained a 32.65% value by using a solid state laser [12].

For what concerns the application of non-conventional materials printed and characterized in the microwave range, in literature it is possible to find examples of coplanar waveguides obtained in Ag and Cu deposited by high-vacuum equipments [13]; microstrip lines realized using Ag microsized flakes dispersed in epoxy resin [14, 15]; thick films realized using high viscosity pastes of Ag and Ag alloys [16]; passive RFID antennas realized by means of inkjet printing and characterized below 2 GHz [17]; metamaterials for the THz regime realized by means of inkjet printing [18]. So far, inkjet printing of nanosized Ag particles on dielectric substrates for RF applications up to 20 GHz has been sparsely reported, see [19].

# 2. Experimental

The raw materials exploited are two kinds of commercial conductive inks, based on a colloidal dispersion of silver NPs in an aqueous medium mixed, respectively, in a glycol/ethanol matrix [12] (InkA-C10/20/30/40, Politronica® Inkjet Printing) and in a UV-curable acrylic polymer (InkA-C100, Politronica® Inkjet Printing). The solid loading of these inks ranges from 16 wt. % (InkA-C100) to 22 wt. % (InkA-C10/20/30/40). Both compositions are specifically formulated for piezoelectric inkjet printing to produce low resistivity and high resolution conductive traces on different kind of substrates. In particular, some of them feature a monomodal distribution of NP diameters, some others a bimodal one (see further Table 1). Inkjet-printed Ag lines were realized using a piezoelectric Jetlab®

4 printer from MicroFab Technologies Inc. equipped with a 60-µm nozzle diameter MJ-AT-01 dispenser. The print head was heated at 60 °C and the substrate at 70 °C on a hotplate during the deposition process, to improve the quality of the deposit [3]; the ink was printed as provided (unfiltered). The waveform used to expel a single droplet was a 35 V pulse lasting 18 µs, followed by a -13 V pulse lasting 36 µs as echo dwell, with the rise/fall/final rise time 25/5/2 µs respectively. The step size was set to 100 µm and 6 layers were printed on top of each other. Sample morphology was studied by high resolution Field Effect Secondary Electron Microscopy (FESEM). The test fixture used to acquire resistance measurements during the hot-plate annealing was made by an aluminum frame, comprised of inspection windows, kapton insulation and K-type thermocouple temperature sensor, that allows the simultaneous characterization of either two samples, using the two point technique, or one sample, using the four point technique.

## 3. Results and discussion

### *Structural and electrical DC characterization*

Gaining control on the ink NP diameter distribution makes it possible, as the main advantage, to indirectly control the sintering characteristics, since a better spatial distribution of particles (like the one obtained by filling a volume with spheres with a bimodal distribution, when compared to a monomodal one), results in an easier sinterization and realization of a full percolating electrical path. The main advantage of changing the ink composition and adding a copolymer, in our case, is connected to gain a control on the heat diffusion through the mass during sintering, resulting in a control over the solvent evaporation.

We point out the main difference when compared to “traditional” inks, whose composition includes solvents, some salt residuals from the incomplete NP formation and metal NPs (C10 to C40) from one side, a copolymer-based composition from the other side. This difference may be seen in Figure 1, where sample sections, obtained after a fragile fracture on a silicon substrate, show what happens during thermal annealing. Panel a) presents a sample of C10 after the annealing procedure, clearly showing that a sponge-like percolating agglomerate of Ag NPs has formed above silicon, while high-boiling temperature solvents are still visible wrapping micrometric agglomerates of Ag NPs on top of the stack. Since the hot-plate annealing is performed leaving free the upper surface of the samples, it is believed that the preferential evaporation path for solvents goes from the film bulk to the upper surface. Nevertheless micro-bubbles are formed during the sinterization and their presence may be witnessed by darker areas on top of the sintered surface (possibly due to crystalline inhomogeneities that scatter / absorb more light) in correspondence of broken bubbles. Bubbles do not break the formation of sintered lines and interfere only before percolation occurrence. Furthermore, bubbles do not form during the sintering of sample C100. Panel b) presents a C100 sample before annealing; its polymeric network traps some solvent droplets and forms a rigid structure through which the solvent evaporation is more controlled, allowing higher heat flows without producing inhomogeneities due to solvent boiling and bubble breaking. Panel c) presents the same sample after annealing, showing the peculiar structure of the percolating network

of Ag NPs and NP agglomerates. Panel d), finally, presents a section of a C10 microstrip printed on polycrystalline alumina substrate, in false color.

Figure 1. FESEM showing sample sections. a) C10 post annealing on silicon (light grey at bottom), on top of the electrically percolating sponge there are solvent residuals wrapping micrometric aggregates of NPs. b) C100 pre annealing on silicon, showing some solvent droplets trapped in the polymeric network. c) C100 post annealing on silicon (grey at bottom), showing the electrically percolating network of Ag NPs embedded in a copolymer matrix. d) C10 (red) post annealing on alumina (light blue).

In order to determine the effective electrical volume of the sample we performed a secondary electron tomography based on the FESEM images of section shown in Figure 1c [20]. This numerical process, based on a calibration experiment, gives the real depth of either a silver NP or an agglomerate of NPs, within a copolymer matrix. Results are shown in Figure 2: after an automated recognition of the NPs caught in a frame [21], each agglomerate is evaluated in terms of mean secondary electron counts, giving to the maximum counts a depth of zero (the NP lies on the fracture plane of the specimen) and to the minimum (still distinguishable from the background corresponding to polymeric matrix without NPs) a depth of 250 nm, producing the depth map in the inset. The value of 250 nm was determined in previous experiments as the maximum distance for an Ag aggregate from a similar copolymer surface to be imaged by our FESEM system. By texture mapping the real FESEM image on the depth data we obtained a representation that helps to compute the volume associated to the NPs and their agglomerates. We could estimate as upper limit that the real Ag volume content in the nanocomposite is 27.56 %, value which is very close to the theoretical percolation threshold as computed in a 2-Dimensional lattice with hexagonal lattice of spherical dispersoids, known to be 31.16 %. The difference between these two values may be easily explained in terms of non-spherical shape of our NP aggregates.

Figure 2. Texture mapped depth distribution of Ag NPs and their aggregates, according to our tomographical reconstruction from FESEM images. All data are in nm. In the inset, absolute depth map, computed from a portion of the image of Figure 1c.

In Figure 3, we show a comparison between the optical absorption spectra of the different inks. By performing multipeak Gaussian fits we obtained the characteristic wavelengths reported in Table 1, together with the corresponding NP size and distributions as obtained through numerical analysis of FESEM images [22], as shown in Figure 4. Starting from a FESEM image of diluted ink on silicon substrate and operating a numerical algorithm, it was possible to extract the true population distribution. In particular, the bimodal distribution of sample C40 depicted in Figure 4 is represented in semilogarithmic scale, since it is composed by a very small number of big NPs and a very high number of small NPs. The complete control over NP diameter distribution is reflected by a complete control over the absorption spectra.

Figure 3. UV-VIS absorption spectra of different Ag NP inks featuring controlled size distributions; multiple Gaussian peak fits associated to the experimental data are shown in continuous lines.

Figure 4. a) FESEM image of C40 diluted in water (20:80), over silicon substrate. b) diameter distribution (in nm) as extracted from a numerical algorithm, whose synthetic grain pattern is represented in the inset; on the vertical scale the absolute number of NPs counted in the frame.

| Ink name | NP diameter main mode x±s [nm][1] | NP diameter mode 2 x±s [nm] [1] | Main peak x±w [nm] [2] | Secondary peak x±w [nm] [2] | Tertiary peak x±w [nm] [2] | Surface resistance [mΩ/□] |
|---|---|---|---|---|---|---|
| C10 (46) | 10 ± 5 | N.A. | 409.7 ± 48.9 | N.A. | N.A. | 30.0 |
| C10 (47) | 15 ± 5 | 100 ± 50 | 400.1 ± 31.0 | 365.9 ± 43.5 | N.A. | 30.0 |
| C10 (52) | 6 ± 2 | 15 ± 5 | 420.5 ± 65.7 | N.A. | N.A. | 30.0 |
| C20 (48) | 25 ± 15 | N.A. | 439.2 ± 77.4 | 555.3 ± 193.2 | 365.9 ± 43.5 | 19.4 |
| C30 (49) | 6 ± 2 | 40 ± 10 | 469.7 ± 115.0 | N.A. | N.A. | 30.0 |
| C40 (41) | 12 ± 2 | 100 ± 50 | 441.0 ± 285.1 | N.A. | N.A. | 22.4 |
| C40 (51) | 12 ± 2 | 100 ± 10 | 470.0 ± 177.6 | N.A. | N.A. | 22.4 |
| C100 (7) | 12 ± 2 | 90 ± 10 | N.A. | N.A. | N.A. | 30.4 |

Table 1. Collection of relevant data for inks according to UV-Vis measurements, FESEM analysis and electrical measurements after annealing.

[1]As determined from numerical analysis of FESEM images, shown the median value ± standard deviation.

[2]As determined from multi-Gaussian fit to UV-Vis spectra, shown peak position ± peak width.

### *Real-time measurements during thermal sintering*

The differences in ink NP size / shape distributions result in a different DC and microwave electrical behavior during and after sintering, as highlighted by the real-time experiments. We could observe a tiny difference between non-disperse and disperse size distributions, consistent with a better spatial close-packing of bimodal distributions, resulting in a percolation threshold reached before monomodal distributions. In order to easily determine the occurrence of electrical percolation, we used as the independent variable the product of temperature and time. Figure 5 shows the outcomes of the real-time experiments, where percolation is obtained after solvent evaporation for all the three samples. Sample C100 features a peculiar slow approach to full sinterization, possibly due to slow solvent evaporation across the polymer network. After reaching the maximum temperature of 330 °C the sample experiences heat flow inversion, since it is let cool down by natural convection; this means that in $T^*t$ coordinates noisy polydromic patterns appear, due to the trade-off between time monotonic increase and temperature local (global) maximum. The graph presented in Figure 5 is obtained according to the following transformation:

$$T^*t = \begin{cases} T \cdot t & if \quad T < T_{Max} \\ T_{Max} \cdot t & if \quad T \geq T_{Max} \end{cases} \tag{1}$$

where the polydromic portion of the function is rectified and converted into a monotonic one. Sintering achievement is evidenced by a green line. After this region, the graph records the cooling branch, reaching resistance minimum. In the inset it is possible to see in detail the improved behavior of sample C100 whose electrical percolation is reached

~$4 \cdot 10^5$ Ks before the other samples. It is even possible to observe the electrical effects of bubble formation during solvent ebullition / evaporation, resulting in a slight resistance increase before percolation occurrence. In particular we could observe bubble formation only when annealing sample C40, in correspondence of the resistive plateau around $10^5$ Ω (Figure 5, inset, red dots / line, only 1 experimental point every 10 is shown).

Figure 5. Real-time resistance experiment output, plotted in bilogarithmic scale as a function of the annealing hardness (temperature times duration), for different ink compositions and NP size distributions. Only 1 experimental point every 10 is shown for clarity. This particular choice of the independent variable allows to easily determine in which conditions we can induce sintering. The electrical percolation threshold is indicated by a steepest resistance drop. In the inset: magnified portion corresponding to electrical percolation threshold.

Most interestingly, we analyzed the same ink under different heating rates. It resulted that the copolymer-based composition is unaffected, at least in the studied range, by the heating rate. Figure 6 presents experimental data together with a numerical fit, in a 3-Dimensional space where the coordinated axes X, Y and Z are time, temperature and log(resistance), respectively. The fit was obtained using Surface Fit Tool of Matlab ® 2010b, choosing a biharmonic function for its smoothness and regular behavior. Data corresponding to the fit allow to realize a complete phase map, useful to project and design new annealing profiles. In particular it is easy to see that for each trajectory on the $t - T$ plane it is always possible to reach the orange part of the surface (low resistance), no matter which path one can choose.

Figure 6. Electrical percolation phase plot for InkA-C100 ink. Black circles: experimental data corresponding to 4 different annealing rates (4, 2, 1 and 0.5 h from the foreground to the background); color surface: biharmonic fit to experimental data. Vertical data (resistance) is presented in log scale.

### *RF and microwave performances*

RF and microwave hybrid circuits typically make use of metallization patterns (needed to implement transmission line components and interconnects) that require complex lithographic processes. Direct printing of high conductivity inks on dielectric substrates, as described in the present work, would be an interesting low-cost alternative, in particular for fast circuit prototyping, also when compared to other techniques based on mechanical or laser milling **ERRORE. L'ORIGINE RIFERIMENTO NON È STATA TROVATA.**. Moreover, since the process is pollution free, it does not require specialized personnel, and disposal of waste with high environment impact. The suitability of the present printed technology for the realization of RF and microwave metallization patterns has been tested through high-frequency characterization of inkjet printed planar transmission lines. To this purpose, several test structures implementing simple microstrip (Figure 7-a) and coplanar lines (Figure 7-b), realized on alumina substrates, have been fabricated and characterized up to 26.5 GHz, in terms of propagation constant, i.e. effective refractive index and attenuation, as a function of frequency.

Figure 7. Microstrip (a) and coplanar stripline (b) layouts.

Following the approach proposed in [24] by some of the authors, these parameters can be accurately extracted starting from the scattering parameter measurements carried out on a pair of test devices with same cross section but different

length. As described in detail in [24], the complex propagation constant of the line can be directly obtained computing the eigenvalues of the matrix represented in eq. 2:

$$T_{L1} \cdot T_{L2}^{-1} \tag{2}$$

where $T_{L1}$ and $T_{L2}$ are the transmission matrices of the pair of test lines; those can be derived from the two measured scattering matrices with simple linear algebraic transformations. The present method, that can be applied to whatsoever waveguide structure, has high numerically robustness also in consideration of the great accuracy provided by modern Vector Network Analyzers (VNAs) **ERRORE. L'ORIGINE RIFERIMENTO NON È STATA TROVATA.**, [26] adopted to measure scattering parameters vs. frequency. The approach only requires the acquired VNA raw data; hence VNA calibration is not needed. This feature is extremely important, since it allows to extract the propagation constant of waveguiding structures for which, as is the present case, calibration kits and standards are not available. The insertion of coaxial connectors at the ends of the lines under characterization (LUTs) would simplify the connection to the VNA. However, that would require to house the substrate on a metallic carrier, and to deal with the contact between connector tips and printed metallic strips where traditional soldering techniques cannot be applied. For these reasons, coplanar lines were directly contacted with high frequency coplanar probes, while microstrip structures were tested adopting the dedicated test-fixture Anritsu 3680K. This setup can be modified to host microstrips with different lengths, and the action of springs, exerting a mechanical force between line endings and coaxial connector tips, ensures that they have a contact with good electrical characteristics up to microwave frequencies.

*RF measurements and comparison with theory*

The measurements have been carried out with a fully automated set-up based on a Agilent VNA, able to provide two port small signal characterization up to 67 GHz, even if the maximum frequency in the present case has been limited to 26.5 GHz. An in-house software controls all the measurements, data acquisition and processing (e.g. VNA raw data calibration when required). To decrease the statistical uncertainty of the measurements, multiple acquisitions (512) and averaging, at each frequency, has been implemented. As outlined before, a pair of lines with same geometry but different lengths can be used for our purposes. However, to validate the procedure, several lines, with identical cross section, but different lengths have been printed so that more pairs could be defined, and independently used for the extraction. Moreover, lines with different widths (320 μm, 630 μm, and 950 μm corresponding to a characteristic impedance higher than 50 Ω, close to 50 Ω and lower than 50 Ω, respectively), printed with three different inks (InkA-C10, InkA-C20, InkA-C40), have been fabricated on alumina substrates.

The extracted attenuation and effective refractive index present a rather non smooth behavior versus frequency mainly due to the somewhat poor repeatability of the external contact with the metallic printed strips, that instead is a strong requirement of the proposed extraction algorithm. This behavior, already visible in microstrip measurements, is more

evident for coplanar lines, since the adopted on-wafer probes are designed for contacting extremely regular and smooth metal surface; in this case the poor quality of the contact (also due to the small probe footprint) limits the proposed extraction up to 5 GHz, the result being too noisy above that frequency.

In order to compare the measured propagation characteristics with a theoretical model, and to indirectly estimate the metal and substrate loss parameters, the lines have been simulated exploiting the microstrip and coplanar stripline models available in the RF and microwave CAD tool Agilent ADS. The metallization conductivity has been initially set at the DC value extracted from the measured 4-point DC resistance of the lines. Then, numerical optimizations were carried out to fit the experimental data, allowing for some uncertainty in the line metallization geometry (length, width and thickness) and of the possible RF deterioration of the metal conductivity. The model also allows for metallization roughness.

Figure 8 reports, for frequencies between 1 and 26.5 GHz, the attenuation and effective refractive index extracted from measurements, and derived from CAD models for microstrips printed with InkA-C10, featuring different widths: $W_1$=630 μm (characteristic impedance close to 50 Ω) and $W_2$=320 μm (impedance around 66 Ω). The agreement between experimental data and simulation is rather good for all the frequency range.

Concerning coplanar striplines, as previously pointed out, the extraction of the attenuation and effective refractive index resulted accurate only up to 5 GHz. Figure 9 shows the extracted and modeled attenuation and the effective refractive index as function of frequency up to 5 GHz. As for microstrips, the agreement between experimental and modeled results is reasonably good.

While the available theoretical models provide a good fit for the line propagation parameters and can therefore the basis for circuit design, some further remarks are required concerning line losses.

In fact, although the modeled RF conductivity is in reasonable agreement with the extracted DC value (see Table 2, columns 3 and 4), significant differences have been observed between the theoretical and optimized value of the alumina substrate loss tangent. While the almost linear trend of the attenuation vs. frequency (as opposed to the square root behavior typical of skin-effect metal losses) suggests the presence of large dielectric losses, the substrate loss tangent required to fit this behavior turns out to be about one order of magnitude larger than the ideal one. Further investigations, that shall be discussed elsewhere, seem to show that deviations from the classical metal attenuation vs frequency behavior, may be ascribed to additional dielectric losses taking place in the printed strips, that cannot be assimilated to silver bulk, but has to be more accurately considered as a composite track of silver NP agglomerates together with the residuals of the evaporation of the ink liquid carrier adopted for printing (see Figure 1).

| Measured | | CAD optimized |
|---|---|---|

| Line width [μm] | Thickness [μm] | σ [S/m] | Charact. Impedance [Ω] | Thickness [μm] | σ [S/m] | tanδ | Roughness [nm] |
|---|---|---|---|---|---|---|---|
| 630 | 2-3 | $2.85 \cdot 10^6$ | ~ 50 | 4.57 | $2.92 \cdot 10^6$ | 0.0133 | 230 |
| 320 | 5-6 | $1.7 \cdot 10^6$ | ~ 66 | 7.41 | $1.5 \cdot 10^6$ | 0.0159 | 630 |

Table 2. Comparison of the averaged DC measured conductivity and corresponding fitted values for the manufactured microstrip lines with width $W_1$=630 μm (characteristic impedance close to 50 Ω) and $W_2$=320 μm (impedance around 66 Ω).The fitted tanδ and roughness are also shown.

In conclusion, concerning the process suitability to RF and microwave hybrid implementation, the line geometrical resolution, repeatability, and accuracy, combined with the exhibited frequency dispersion and losses, are satisfactory enough to make this technology compatible up to a few gigahertz to all RF applications not requiring high-Q components. The measured attenuations of microstrip lines are comparable or better than the attenuations reported in [19] for inkjet printed coplanar lines on glass substrates (1.62 dB/cm at 10 GHz and 2.65 dB/cm at 20 GHz, respectively).

Figure 8. Extracted attenuation and effective refractive index (black)of a microstrip line with width $W_1$=630 μm (characteristic impedance close to 50 Ω), and of a microstrip line with width $W_2$=320 μm (impedance around 66 Ω) (blue). The solid lines refer to the corresponding quantities as calculated from the model simulations.

Figure 9. Extracted attenuation (blue squares) and effective refractive index (blue crosses) of a coplanar line with width W=200 μm, $W_{ground}$=10 mm and spacing between the lines S=200 μm (characteristic impedance higher than 50 Ω). The solid lines refer to the corresponding quantities as calculated from the model simulations.

## 4. Conclusions

In conclusion we explored the effects of NP diameter distribution and composition of Ag NP-based inks for the realization of inkjet printed microwave circuits. By means of a real-time experiment we found a surprising behavior of a specific composition, an ink added by a copolymer, able to produce an extremely conductive line even by increasing the heating rate four folds. The FESEM analysis showed a peculiar nanocomposite structure with a percolating network of NP agglomerates, having an extremely low true density of noble metal into the polymeric network. The microwave characterization performed up to 26.5 GHz showed that microstrip and coplanar waveguides inkjet printed with Ag NP-based formulations are compatible with applications up to 20 GHz.

## Acknowledgements

The authors would like to thank Dr. Ignazio Roppolo and Prof. Marco Sangermano of Politecnico di Torino and Dr. Paola Del Grosso for their useful help.

## 5. References


[1] H.-H. Lee, K.-S. Chou, K.-C. Huang, Nanotechnology 16 (2005) 2436;

[2] K.C. Yung, S.P. Wu, H. Liem, J. Mater. Sci. 4 (2009) 154;

[3] J. Perelaer, B.-J. de Gans, U.S. Schubert, Adv. Mater. 18 (2006) 2101;

[4] U. Caglar, K. Kaija, P. Mansikkamaki, Proc. 2008 2nd IEEE Int. Nanoelectron. Conf. 851;

[5] A. Scandurra, G. F. Indelli, N.G. Spartà, F. Galliano, S. Ravesi, S. Pignataro, Surf. Interface Anal. 42 (2010) 1163;

[6] J.G. Bai, K.D. Creehan, H.A. Kuhn, Nanotechnology 18 (2007) 185701;

[7] I. Reinnhold, C.E. Hendriks, R. Eckardt, J.M. Kranenburg, J. Perelaer, R.R. Baumann, U.S. Schubert, J. Mater. Chem. 19 (2009) 3384;

[8] M. Allen, A. Alastalo, M. Suhonen, T. Mattila, J. Leppäniemi and H. Seppä, IEEE Transactions on Microwave Theory and Techniques. 59 (2011) 1419-1429,

[9] S. Magdassi, M. Grouchko, O. Berezin, A. Kamyshny, ACS Nano 4 (2010) 1943;

[10] J. Perelaer, C.E. Hendriks, A.W.M. de Laat, U.S. Schubert, Nanotechnology 20 (2009) 165303;

[11] I. Kim, Y.A. Song, H.C. Yung, J.W. Joung, S.-S. Ryu, J. Kim, J. Electron. Mater. 37 (2008) 1863;

[12] A. Chiolerio, G. Maccioni, P. Martino, M. Cotto, P. Pandolfi, P. Rivolo, S. Ferrero, L. Scaltrito, Microelectron. Eng. 88 (2011) 2481;

[13] V.V. Levenets, R.E. Amaya, N.G. Tarr, T.J. Smy, J.W.M. Rogers, IEEE Electron Device Letters 26 (2005) 357;

[14] T. Björninen, S. Merilampi, L. Ukkonen, P. Ruuskanen, L. Sydänheimo, IET Microw. Antennas Propag. 4 (2010) 1224;

[15] S.M. Wentworth, B.L. Dillaman, J.R. Chadwik, C.D. Ellis, R.W. Johnson, IEEE Trans. on Components, Packaging, and Manufacturing Tech. 20 (1997) 52;

[16] K. Pitt, C. Free, Z. Tian, M. Jakubowska, J. Mater. Sci.: Materials in Electronics 12 (2001) 491;

[17] A. Rida, L. Yang, R. Vyas, M.M. Tentzeris, IEEE Antennas and Propagation Magazine 51 (2009) 13;

[18] M. Walther, A. Ortner, H. Meier, U. Löffelman, P.J. Smith, J.G. Korvink, Appl. Phys. Lett. 95 (2009) 251107;

[19] O. Azucena, J. Kubby, D. Scarbrough, C. Goldsmith, "Inkjet printing of passive microwave circuitry," Microwave Symposium Digest, 2008 IEEE MTT-S International , vol., no., pp.1075-1078, 15-20 June 2008

[20] A. Chiolerio, M. Sangermano, Mater. Sci. & Eng. B, 177 (2012) 373-380;

[21] A. Chiolerio, L. Vescovo, M. Sangermano, Macromol. Chem. Phys. 211 (2010) 2008;

[22] A. Virga, P. Rivolo, E. Descrovi, A. Chiolerio, G. Digregorio, F. Frascella, M. Soster, F. Bussolino, S. Marchiò, F. Geobaldo, F. Giorgis, J. Raman Spectr. (2011) DOI: 10.1002/jrs.3086;

[23] D.T. Pham, S.S. Dimov, P.V. Petkov and T. Dobrev, Laser milling as a ‘rapid’ micromanufacturing process. *Proceedings of the I MECH E Part B. Journal of Engineering Manufacture*, 218 1 (2004), pp. 1–7.

[24] G.Ghione, M.Goano, G. Madonna, G.Omegna, M.Pirola, “Microwave modeling and characterization of thick coplanar waveguides on oxide-coated lithium Niobate substrates for electro-optical applications”, *Proc. IEEE MTT-s Int. Microwave Symp. Dig.1999*, pp. 1007-1010

[25] M. Pirola, V. Teppati, V. Camarchia, "Microwave Measurements Part I: Linear Measurements," *IEEE Instrumentation & Measurement Magazine*, Vol. 10-2, pp. 14-19, 2007.

[26] V. Camarchia, V. Teppati, S. Corbellini and M. Pirola, "Microwave Measurements – Part II - Non-Linear Measurements", *IEEE Instrumentation & Measurement Magazine*, Vol. 10, no. 3, June 2007, pp. 34-39.

## *Figures*

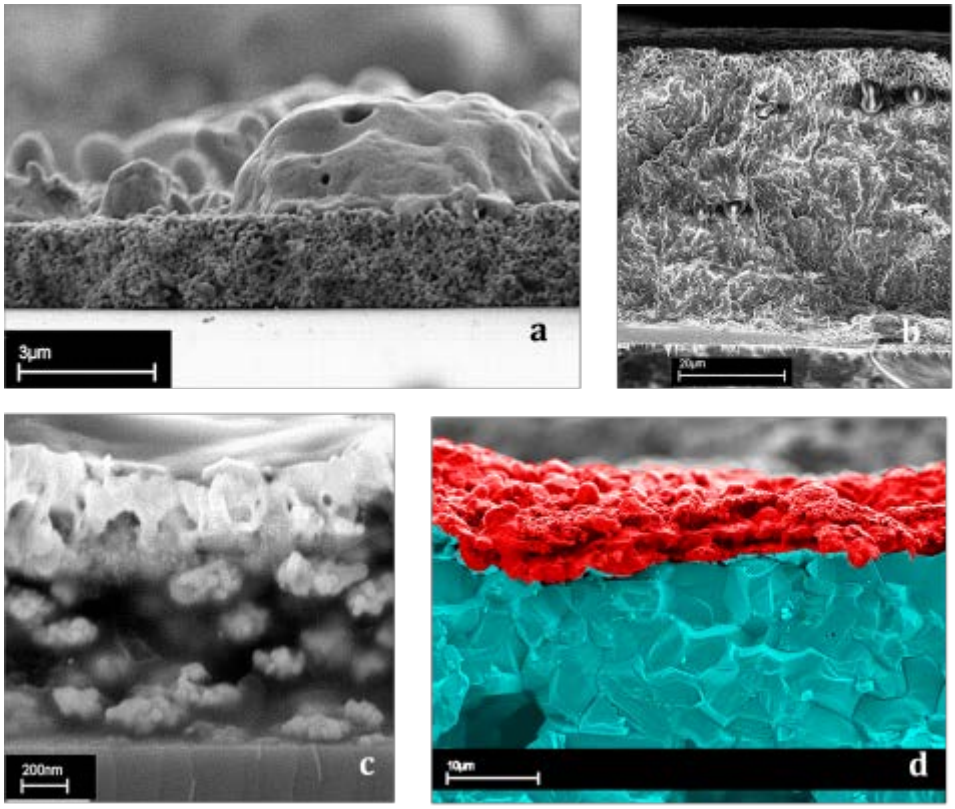
3μm
a
b
200nm
c
10μm
d

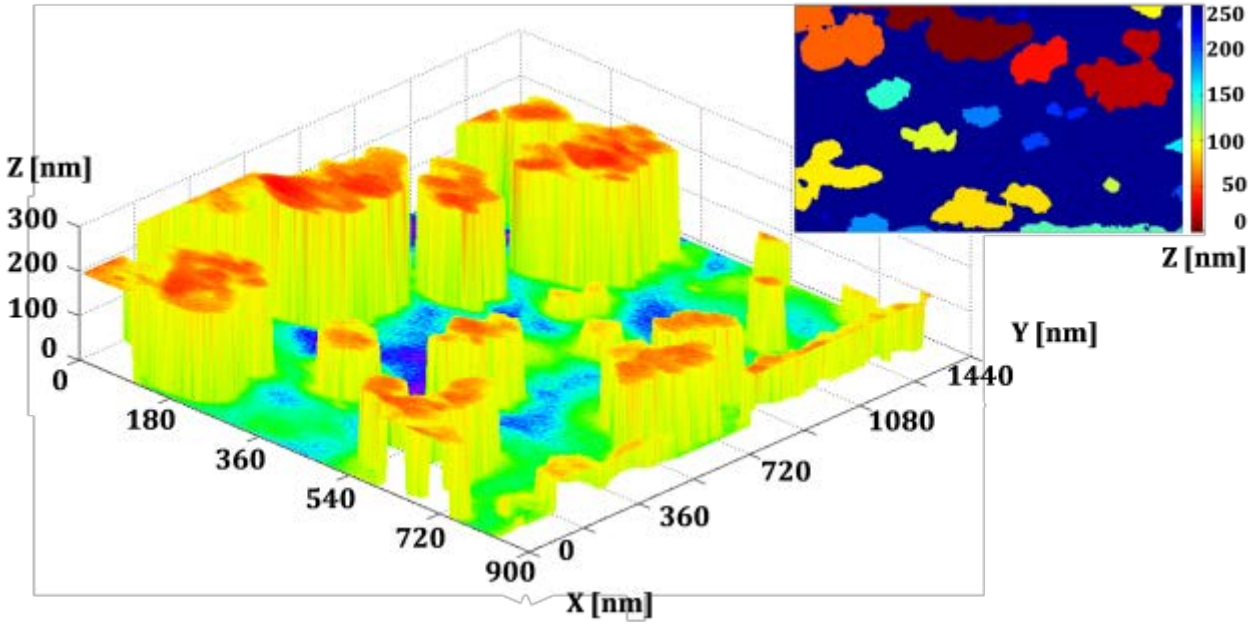
Z [nm]
300
200
100
0
0
180
360
540
720
900
X [nm]
0
360
720
1080
1440
Y [nm]
250
200
150
100
50
0
Z [nm]

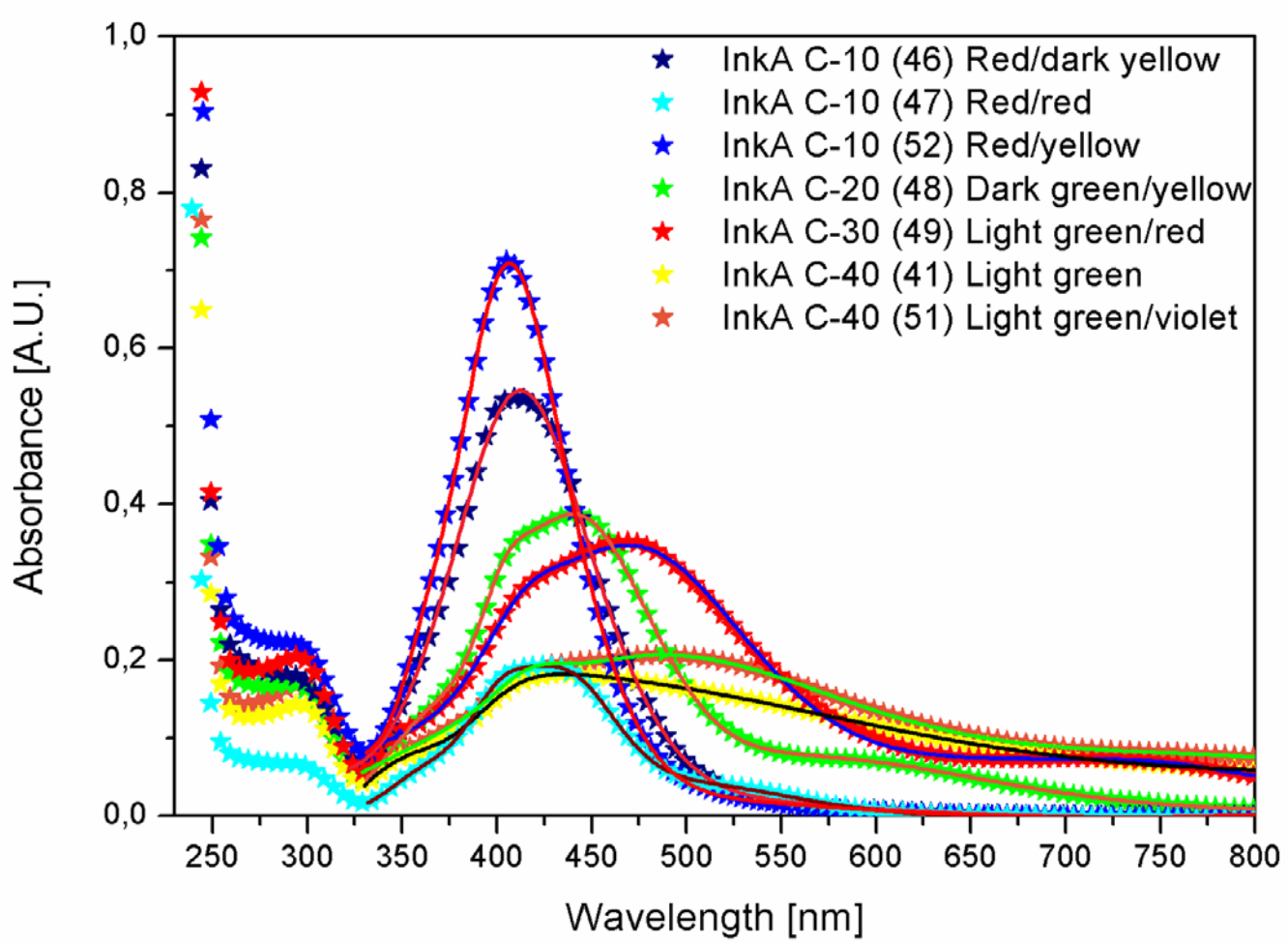
InkA C-10 (46) Red/dark yellow
InkA C-10 (47) Red/red
InkA C-10 (52) Red/yellow
InkA C-20 (48) Dark green/yellow
InkA C-30 (49) Light green/red
InkA C-40 (41) Light green
InkA C-40 (51) Light green/violet
Absorbance [A.U.]
Wavelength [nm]
1,0
0,8
0,6
0,4
0,2
0,0
250
300
350
400
450
500
550
600
650
700
750
800

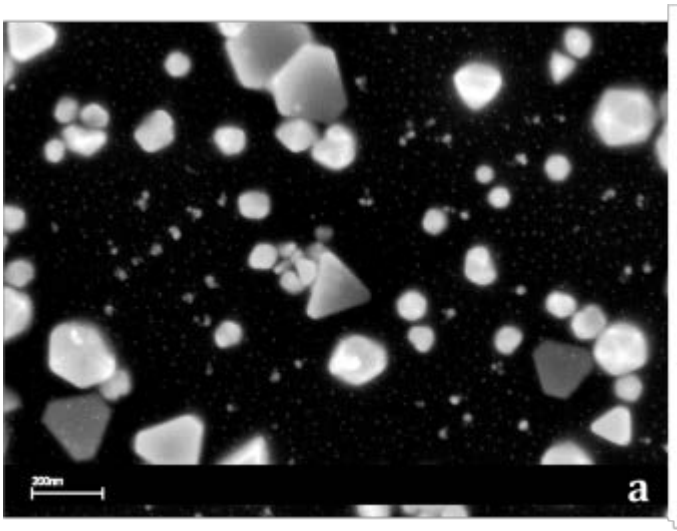
a

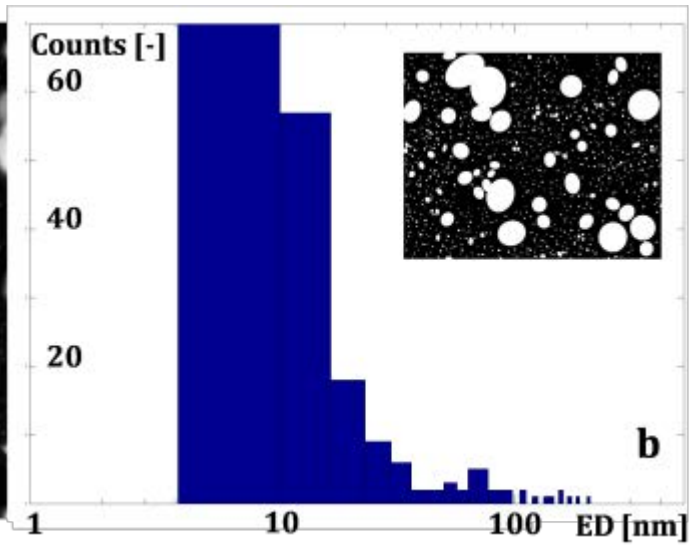
Counts [-]
60
40
20
b
1
10
100
ED [nm]

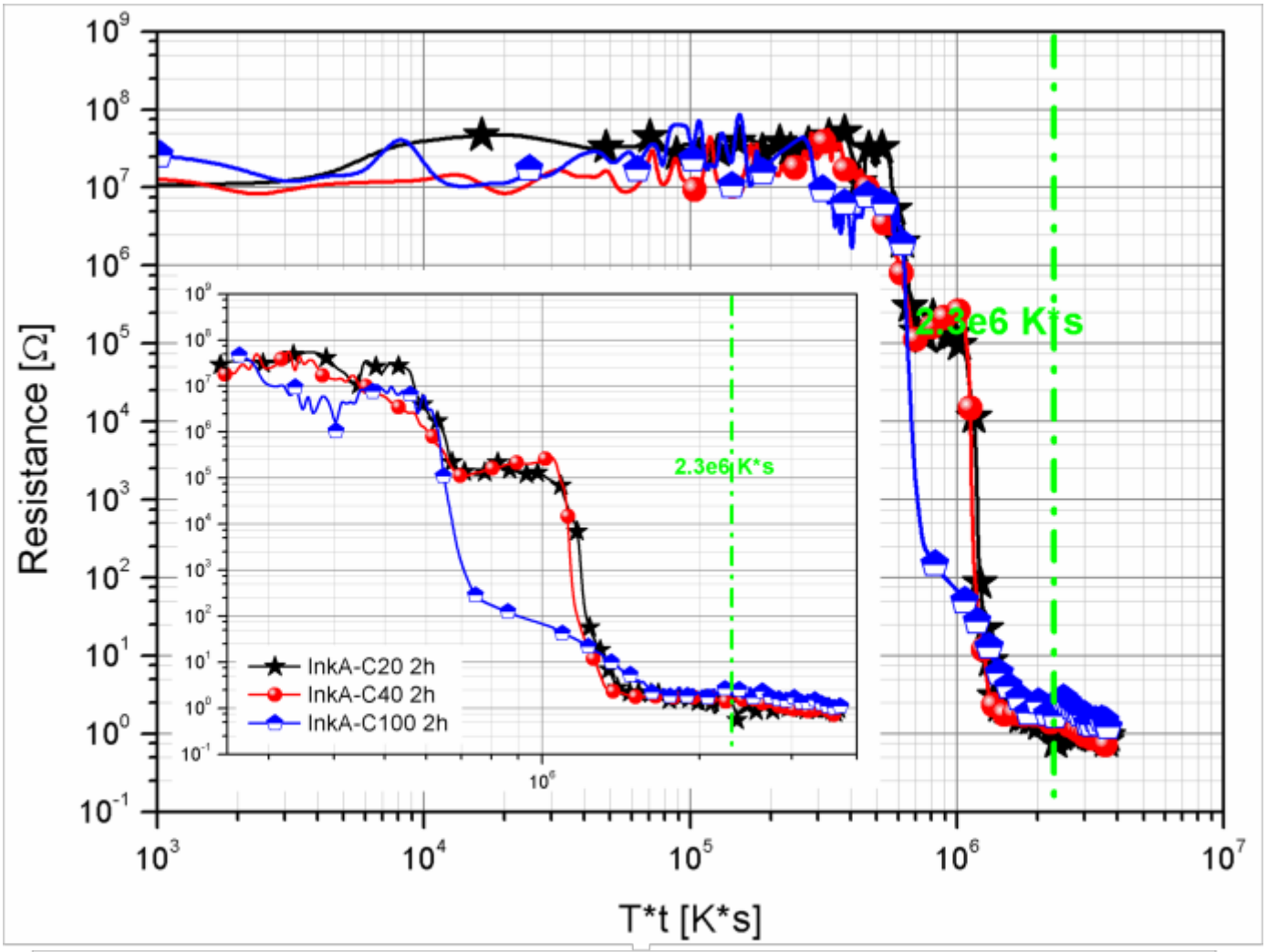
Resistance [Ω]
T*t [K*s]
2.3e6 K*s
2.3e6 K*s
InkA-C20 2h
InkA-C40 2h
InkA-C100 2h

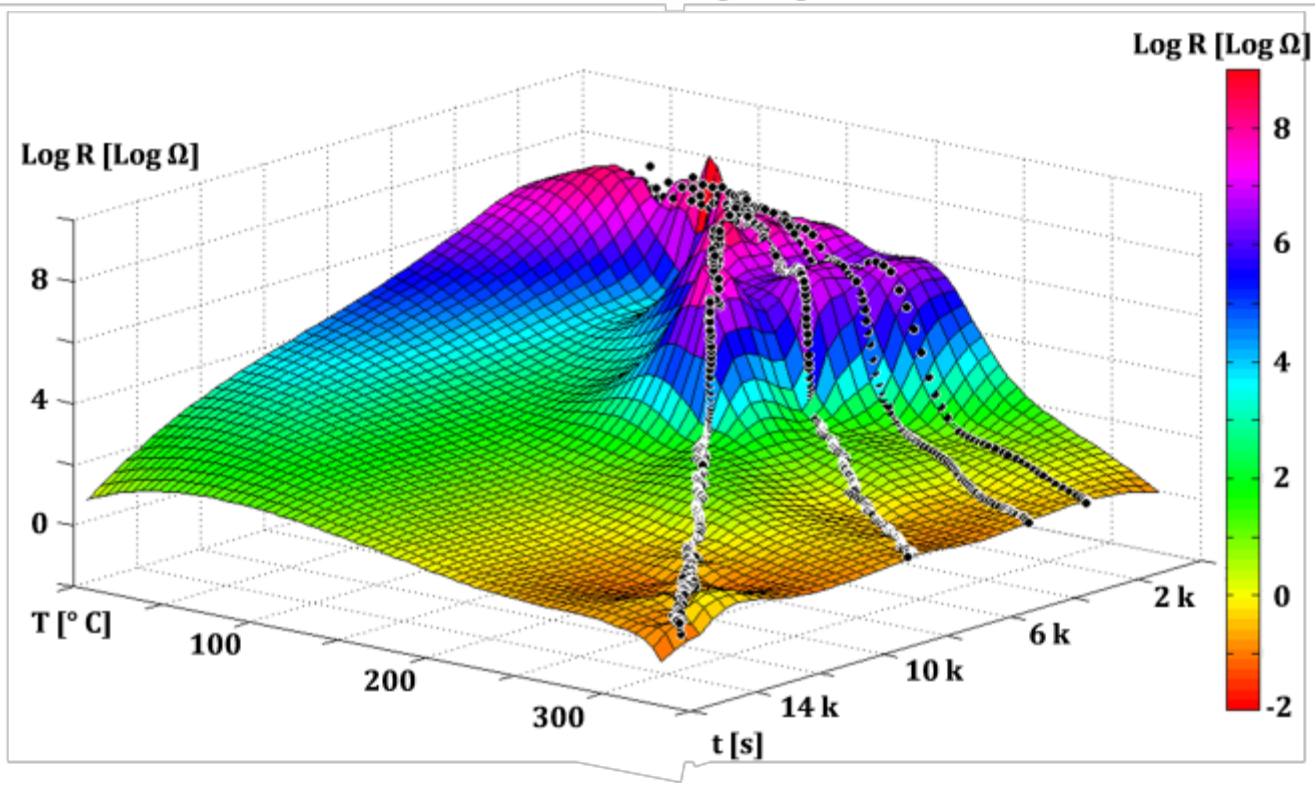
Log R [Log Ω]
Log R [Log Ω]
T [° C]
100
200
300
t [s]
2 k
6 k
10 k
14 k

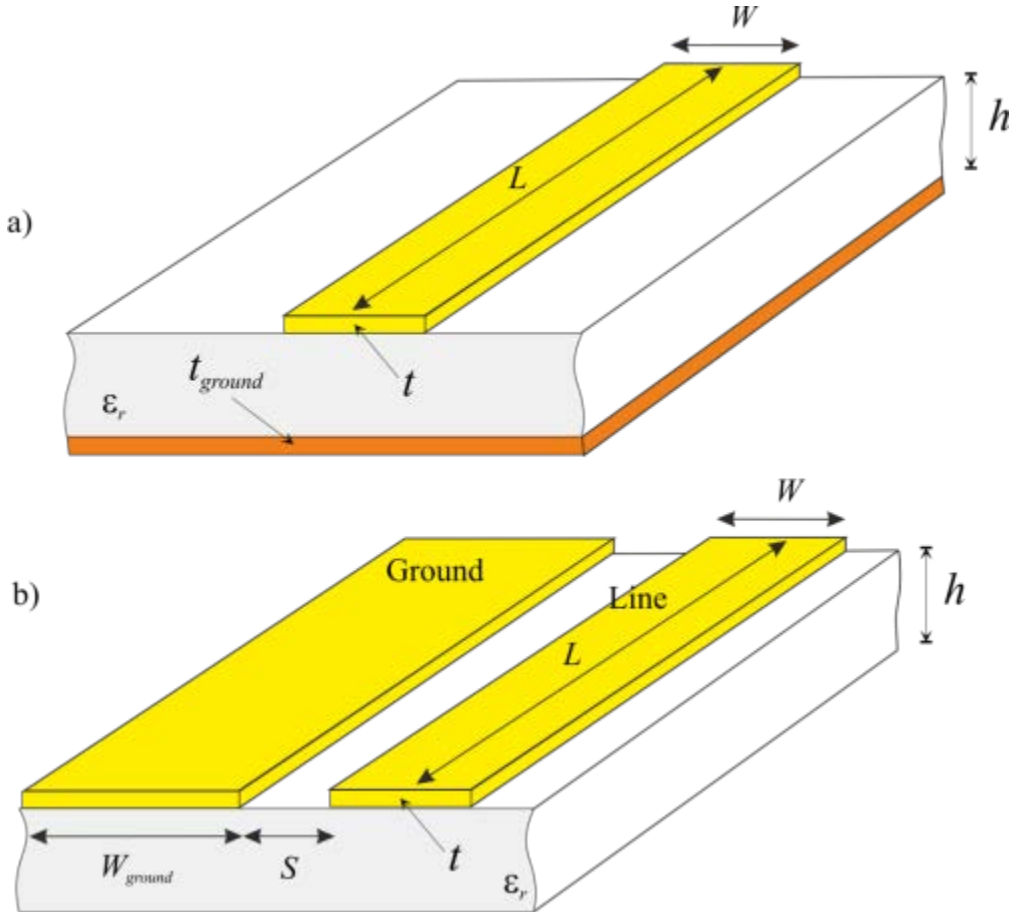
a)
W
h
L
$t_{ground}$
t
$\varepsilon_r$
b)
W
Ground
Line
h
L
$W_{ground}$
S
t
$\varepsilon_r$

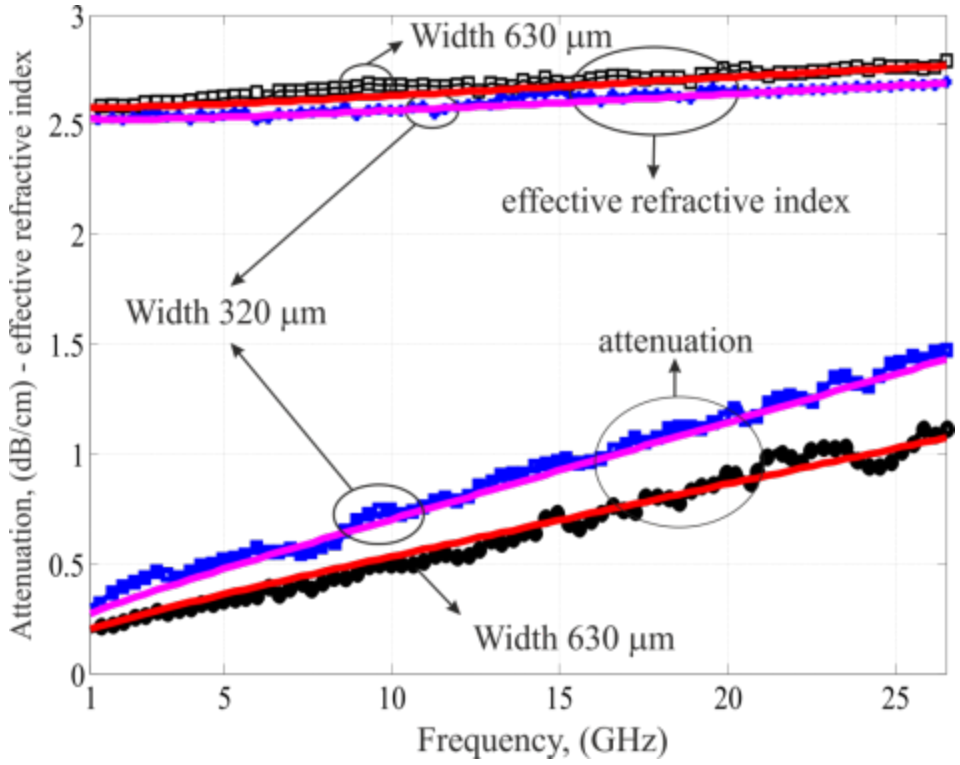
Width 630 µm
effective refractive index
Width 320 µm
attenuation
Width 630 µm
Attenuation, (dB/cm) - effective refractive index
Frequency, (GHz)
0
0.5
1
1.5
2
2.5
3
1
5
10
15
20
25
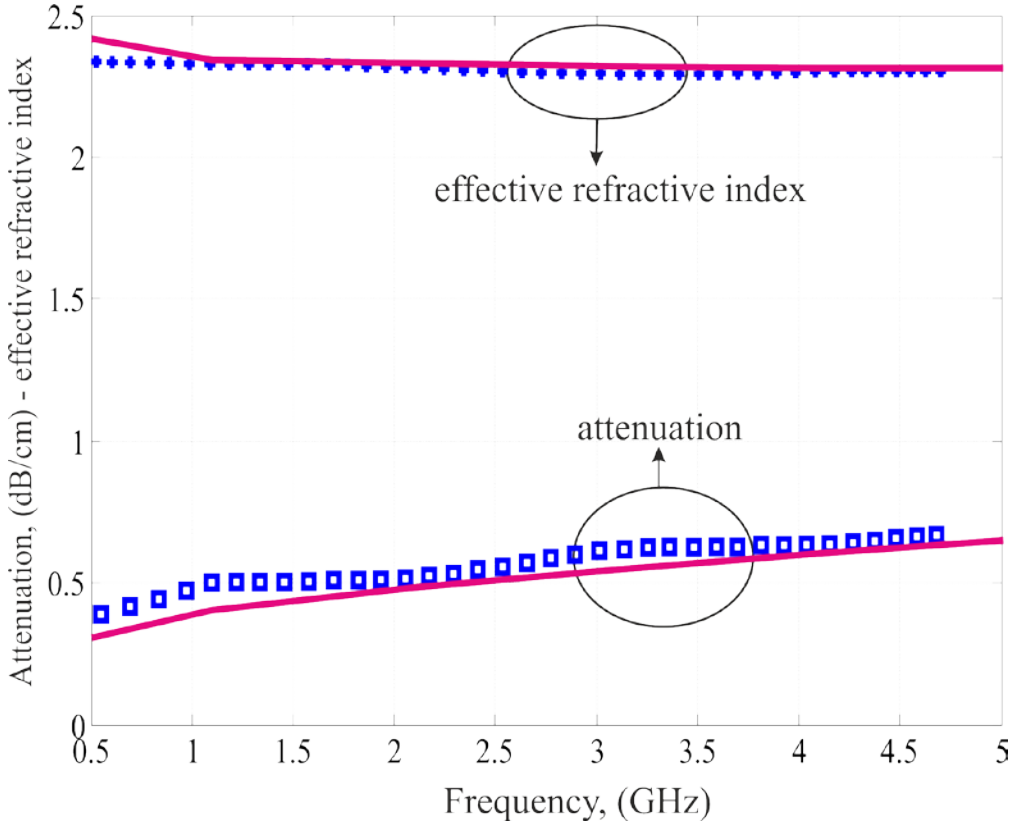
*Ag NP-copolymer nano composite*